Chinese Journal of
POLYMER SCIENCE

RESEARCH ARTICLE

https://doi.org/10.1007/s10118-025-3529-x
Chinese J. Polym. Sci. **2026**, *44*, 756–767

Revisiting the Effect of Reactive Compatibilization on Polymer Crystallization: From Static Suppression to Shear-induced Promotion

Bao-Gou Wu[a,b], Xiao-Hu Bing[a,b], Qian Ren[a], Lan Ding[a], Ji-Zhang Li[a], Wen-Ge Zheng[a,b], and Long Wang[a,b*]

[a] *Ningbo Key Lab of Polymer Materials, Ningbo Institute of Materials Technology and Engineering, Chinese Academy of Sciences, Ningbo 315201, China*
[b] *University of Chinese Academy of Sciences, Beijing 100049, China*

Electronic Supplementary Information

Abstract Reactive compatibilization has been widely applied to enhance the compatibility of polymer blends, thereby improving their mechanical properties. However, it generally reduces the chain mobility and regularity, often leading to slower polymer crystallization. Here, we demonstrate that reactive compatibilization in poly(lactic acid)/poly(butylene adipate-*co*-terephthalate) (PLA/PBAT) blends unexpectedly promotes PLA matrix crystallization during injection molding, in contrast to the retarded kinetics observed in differential scanning calorimetry isothermal crystallization studies. The phase morphology, rheological behavior, and crystalline structure were systematically analyzed to elucidate markedly different crystallization kinetics under static and shear fields. The potential mechanism underlying crystallization enhancement is attributed to PBAT domain refinement and viscosity increase induced by reactive compatibilization, which, under shear flow, create favorable conditions for crystallization by enhancing PBAT fibril nucleation and retarding the relaxation of oriented PLA chains. This study offers new perspectives on the effect of reactive compatibilization on the polymer crystallization behavior.

Keywords Reactive compatibilization; Crystallization; Static field; Shear flow field

Citation: Wu, B. G.; Bing, X. H.; Ren, Q.; Ding, L.; Li, J. Z.; Zheng, W. G.; Wang, L. Revisiting the effect of reactive compatibilization on polymer crystallization: from static suppression to shear-induced promotion. *Chinese J. Polym. Sci.* **2026**, *44*, 756–767.

INTRODUCTION

Blending two polymers can achieve complementary mechanical properties, thereby enhancing the overall performance of the blend system.[1–6] However, owing to differences in the solubility parameters, most polymer blends exhibit poor compatibility, which limits the effective exploitation of their complementary characteristics.[7–11] Therefore, it is critical to improve the compatibility of polymer blends. Reactive compatibilization enables the *in situ* generation of graft copolymers containing chains from both polymers during blending, significantly improving compatibility, and has thus become a widely adopted strategy for polymer blend modification.[12–16] Nonetheless, these branched graft copolymers often reduce the mobility and regularity of the polymer chains, consequently slowing their crystallization rate.[12,17–19]

Taking the widely studied bio-based and biodegradable polylactic acid (PLA) as an example, although PLA exhibits a relatively high mechanical strength, its toughness is insufficient.[20–23] To improve PLA toughness, flexible polymers are often introduced in combination with reactive compatibilization.[17,24–28] For example, Ma *et al*.[17] incorporated ethylene-vinyl acetate-glycidyl methacrylate (EVMG) elastomers in the poly(L-lactide) (PLLA) matrix, where the epoxy groups of EVMG reacted with the hydroxyl and carboxyl end groups of PLLA, *in situ* forming EVMG-*g*-PLLA graft copolymers. This reaction significantly improves the compatibility and enhances the impact toughness of PLLA. However, it also suppressed PLLA crystallization, increasing the half-crystallization time at 130 °C from 28.8 min to 34.8 min. Similarly, in our recent study on PLA/poly(butylene adipate-*co*-terephthalate) (PBAT) blends,[18] the introduction of an epoxy chain extender (ADR) as a reactive compatibilizer led to the *in situ* generation of PLA-*co*-PBAT copolymers during melt blending, improving the toughening efficiency of PBAT while simultaneously slowing the crystallization of the PLA matrix. Li *et al*.[19] further confirmed that reactive compatibilization inhibits PLA crystallization in PLA/PBAT blends. However, it is worth noting that these findings are based on experiments under static conditions (*e.g.*, differential scanning calorimetry isothermal crystallization or compression molding), and systematic studies on the effect of reactive compatibilization on polymer crystallization under flow fields remain scarce.

Previous studies have shown that flow fields (*e.g.*, shear flow generated during injection molding) can induce polymer chain orientation, resulting in more ordered chain segments that facilitate nucleation and crystal growth, thereby promoting polymer crystallization.[29–32] However, at the crys-

* Corresponding author, E-mail: wanglong@nimte.ac.cn
Received November 7, 2025; Accepted December 9, 2025; Published online February 4, 2026

tallization temperature of polylactic acid (PLA), that is, exceeding its glass transition temperature (T_g), the relaxation time of its molecular chains is short, causing rapid disorientation of the chains and significantly limiting the crystallization-promoting effect.[29,31] Li *et al.*[31] reported that the introduction of PBAT can extend the relaxation time of PLA chains, thereby suppressing chain disorientation, while fibrillar PBAT formed under shear flow functions as a heterogeneous nucleating agent, and the combination of these effects synergistically enhances PLA crystallization. Moreover, Chen *et al.*[33] demonstrated that during injection molding of PLA/poly(butylene succinate-*co*-adipate) (PBSA) blends, strong shear flow leads to the generation of PBSA fibrils, which serve as "shish" to promote the ordered arrangement of PLA lamellar crystals, ultimately resulting in a unique "hybrid shish-kebab" structure. Nevertheless, these studies have primarily focused on the crystallization behavior of pristine blends under shear flow, leaving the effect of reactive blend systems largely unexplored.

In this study, we investigated the crystallization behavior of reactive compatibilized PLA/PBAT blends under shear flow generated during injection molding, with the goal of elucidating the effect of reactive compatibilization on polymer crystallization in flow fields. Surprisingly, under shear flow, reactive compatibilization not only failed to suppress PLA crystallization but actually promoted it. The underlying mechanism responsible for this crystallization enhancement was clarified through systematic analysis of the blend morphology, rheological behavior, and crystal structure. This study provides a new understanding of the crystallization behavior of reactive compatibilised polymer blends.

EXPERIMENTAL

Materials

PLA (L175) with an optical purity of about 99% and a weight-average molecular weight of 2.14×10^5 g/mol (polydispersity index of 1.7) was obtained from Total Corbion. PBAT (TH801T) was purchased from the Xinjiang Blue Ridge Tunhe. Joncryl ADR-4468 (ADR), an epoxy-functional styrene-acrylic oligomer with a molecular weight of 7250 g/mol and epoxy equivalent weight of 310 g/mol, was supplied by BASF.

Sample Preparation

Prior to melt blending, PLA and PBAT pellets were dried overnight at 60 °C in a vacuum oven. Melt blending of PLA, PBAT, and ADR was performed using an SHL-52 co-rotating twin-screw extruder at barrel temperatures of 160–190 °C from the hopper to the die, with a screw speed of 40 r/min. PLA/PBAT mass ratios of 95/5, 90/10, and 85/15 were fabricated with a fixed ADR content of 1 phr and designated as B5A1, B10A1, and B15A1, respectively. For comparison, neat PLA, PLA/PBAT (90/10), and PLA/ADR (100/1) were fabricated following the same processing procedure and are labeled as PLA, B10A0, and B0A1, respectively. The compositions of all blends are listed in Table 1. The extrudates were cooled in a water bath, granulated, and dried. The resulting pellets were injection molded into specimens using a Systec 100/420–310C injection molding machine at a barrel temperature of 200 °C and an injection speed of 90 mm/s. The molded parts, having a dumbbell shape and 3 mm thickness, were obtained in a mold maintained at 100 °C and left in the mold for 2 min before ejection.

Table 1 Composition of PLA and its blends.

Sample	PLA (phr)	PBAT (phr)	ADR (phr)
PLA	100	0	0
B10A0	90	10	0
B0A1	100	0	1
B5A1	95	5	1
B10A1	90	10	1
B15A1	85	15	1

Characterization

Differential scanning calorimetry (DSC)

The isothermal crystallization behavior of the extruded pellets under nitrogen atmosphere was investigated using DSC. The samples were initially heated to 200 °C and held for 3 min to eliminate their thermal history and were then cooled to 90, 100, 110, and 120 °C at 50 °C/min, respectively. Isothermal crystallization was then conducted until complete crystallization was achieved.

For the injection-molded specimens, DSC first-heating scans were employed to determine the PLA crystallinity (X_c) of the skin and core layers. In this experiment, the skin layer was defined as a 0.5 mm-thick region at the surface of the injection-molded bar, and the core layer was defined as the 1 mm thick region at its center, as shown in Fig. S1 (in the electronic supplementary information, ESI). The samples were heated from 20 °C to 200 °C at 10 °C/min, and the X_c was calculated as detailed in ESI.

Scanning electron microscopy (SEM)

The phase and crystalline morphologies were observed using an S-4800 SEM operated at 4 kV. To characterize the phase morphology, the injection-molded specimens were cryogenically fractured with the fracture surfaces oriented parallel or perpendicular to the melt flow direction. To observe the crystalline morphology, the cryo-fractured specimens were etched in a methanol-water-sodium hydroxide solution (14 mL: 6 mL: 20 mg) at room temperature for 1.5 h to preferentially dissolve the amorphous PLA regions. Prior to SEM observation, all the samples were coated with a platinum layer.

Polarized Fourier transform infrared spectroscopy (P-FTIR)

To verify that the molecular chains could be oriented by a shear flow field, a NICOLET 6700 P-FTIR instrument equipped with a polarizer was utilized. The spectra were recorded in the reflection mode with 32 scans at a resolution of 4 cm^{-1}. Multiangle scanning was conducted by varying the polarizer angle from 0° to 180° at intervals of 5°. The dichroic ratio (D) and orientation factor (f) were calculated using the following equations:[34]

$$D = A_{\parallel}/A_{\perp} \quad (1)$$

$$f = (D - 1) / (D + 2) \quad (2)$$

where $A_{\parallel}$ and $A_{\perp}$ are the parallel and perpendicular absorbance, respectively. The orientation of the amorphous phase was determined from the absorption band at 956 cm^{-1}.[35]

Rheology behavior

The extruded PLA and its blends were hot-pressed into discs (1 mm thickness, 25 mm diameter) at 200 °C and 10 MPa for dy-

namic rheological experiments. Rheological behavior was analyzed at 190 °C using an HR-3 ARES rotational rheometer, with frequency sweeps ranging from 0.01 rad/s to 100 rad/s under a constant strain of 1%.

Two-dimensional wide-angle X-ray diffraction (2D-WAXD) 2D-WAXD analysis was performed using an Xeuss 3.0 X-ray diffractometer to examine the oriented crystalline structure. An X-ray beam with a wavelength of 0.154 nm was focused onto a circular area with a diameter of 500 μm and a sample-to-detector distance of 50 mm. Sample dimensions of 10 mm × 3 mm × 1 mm were sectioned from the mid-region of the injection-molded bar, as illustrated in Fig. S1 (in ESI). The X-ray beam was aligned perpendicular to the MD-ND plane, with its center positioned 500, 1000, and 1500 μm below the MD-TD surface. The WAXD intensity profiles as functions of 2θ were acquired by integrating the azimuthal angles from 0° to 360° across the 2D-WAXD patterns. The azimuthal scan profiles were obtained by integrating the diffraction intensities azimuthally at the 2θ angle corresponding to the PLA (200/110) lattice plane reflection. Herman's orientation factor (f_H) was determined as detailed in ESI.

RESULTS AND DISCUSSION

Isothermal Crystallization Behaviors

The isothermal crystallization behaviors of PLA and its blends at 90–120 °C were investigated using DSC. The DSC curves are shown in Fig. S2 (in ESI), and the corresponding relative crystallinity-time curves are shown in Figs. 1(a)–1(d). These curves were used to determine the half-crystallization time ($t_{1/2}$, defined as the time required to achieve 50% relative crystallinity)[36] which reflects the crystallization rate and is summarized in Fig. 1(e). At the crystallization temperatures of 90 and 100 °C, the B10A0 blend exhibited a shorter $t_{1/2}$ than that of neat PLA. For instance, the $t_{1/2}$ at 90 °C decreases from 6.22 min for neat PLA to 5.08 min for B10A0, indicating that PBAT had a heterogeneous nucleation effect and accelerated the crystallization of the PLA matrix.[37] However, at the higher temperatures of 110 and 120 °C, the $t_{1/2}$ of the B10A0 blend was longer than that of neat PLA, which may be attributed to the increased molecular chain mobility of PBAT near its melting point (120.0 °C, see the DSC curve of PBAT in Fig. S3 in ESI), leading not only to nucleation failure but also to disruption of the ordered stacking of PLA crystalline nuclei. For the B0A1 and B10A1 blends, the $t_{1/2}$ across the entire temperature range of 90–120 °C was significantly longer than that of neat PLA. Specifically, the $t_{1/2}$ at 100 °C increases from 2.20 min for neat PLA to 3.52 min for B0A1 and 4.39 min for B10A1. This is attributed to the reaction between the epoxy groups of ADR and the terminal groups (carboxyl and hydroxyl) of PLA, which induces chain branching or even partial crosslinking of PLA, thereby reducing the chain regularity and mobility, and ultimately decreasing the crystallization rate of PLA.[12,18,38]

Crystallinity of the Injection-molded Specimens

The crystallinity of the skin and core layers in injection-molded PLA and its blends, which were held in the mold at 100 °C for 2 min, was examined. The DSC curves are shown in Figs. 2(a) and 2(b), the thermal parameters are listed in Tables S1 and S2 (in ESI), and the corresponding crystallinity values are summarized in Fig. 2(c). The B10A0 blend exhibited higher crystallinity than neat PLA in both layers, consistent with its faster crystallization rate at 100 °C observed in the DSC isothermal crystallization results. Unexpectedly, the B10A1 blend, which demonstrated a markedly slower crystallization rate than neat PLA in the DSC isothermal crystallization analysis, displayed the highest crystallinity in both layers among all injection-molded samples. For

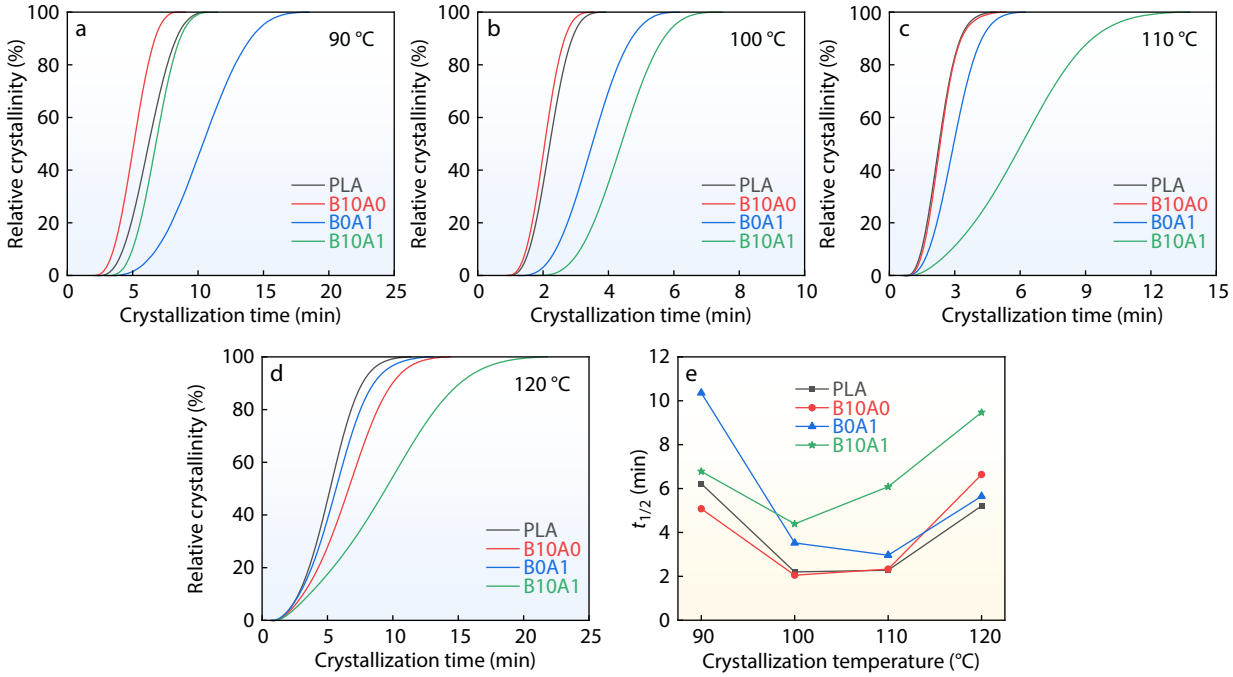

Fig. 1 Variation of relative crystallinity versus crystallization time for PLA and its blends isothermally crystallized at (a) 90 °C, (b) 100 °C, (c) 110 °C, and (d) 120 °C; (e) Summary of the half-crystallization time.

https://doi.org/10.1007/s10118-025-3529-x

instance, the skin layer of the B10A1 specimen exhibited no cold crystallization and attained a high crystallinity of 41.6%, whereas that of the neat PLA showed only 11.9% crystallinity. To the best of our knowledge, this unusual phenomenon has not yet been reported. Similarly, the B0A1 blend, which also exhibited slower crystallization kinetics than PLA, showed marginally higher skin-layer crystallinity than PLA, despite a lower core-layer crystallinity. Additionally, all the samples exhibited higher crystallinity in the skin layer than in the core layer. The underlying crystallization mechanism is elucidated in the following sections.

Phase Morphology

To clarify the reasons behind the discrepancy between the crystallinity trends observed in the aforementioned injection-molded specimens and the DSC isothermal crystallization results, particularly the unexpectedly high crystallinity of the B10A1 specimens, the phase morphologies of the B10A0 and B10A1 blends were examined, as shown in Fig. 3. For the B10A0 specimen, the cross-sectional morphology perpendicular to the flow direction exhibited a typical sea island structure, where the PBAT phase was dispersed as spherical domains within the PLA matrix. Owing to the limited compatibility between PBAT and PLA, a well-defined phase interface was present. Interestingly, in the cross-section parallel to the flow direction, the PBAT phase appeared as a fibrillar structure, which can be attributed to the shear flow field generated during injection molding.[38–40] Compared to spherical PBAT domains, the fibrillar PBAT structure possesses a higher specific surface area, which is more favorable for heterogeneous nucleation.[31] Moreover, because the skin layer of the injection-molded specimen is subjected to stronger shear than the core layer, the PBAT fibrils in the skin region are significantly longer than those in the core.[40] The PBAT phase morphology in the B10A1 specimen was similar to that in the B10A0 specimen in both the perpendicular and parallel sections relative to the flow direction. However, in B10A1, the

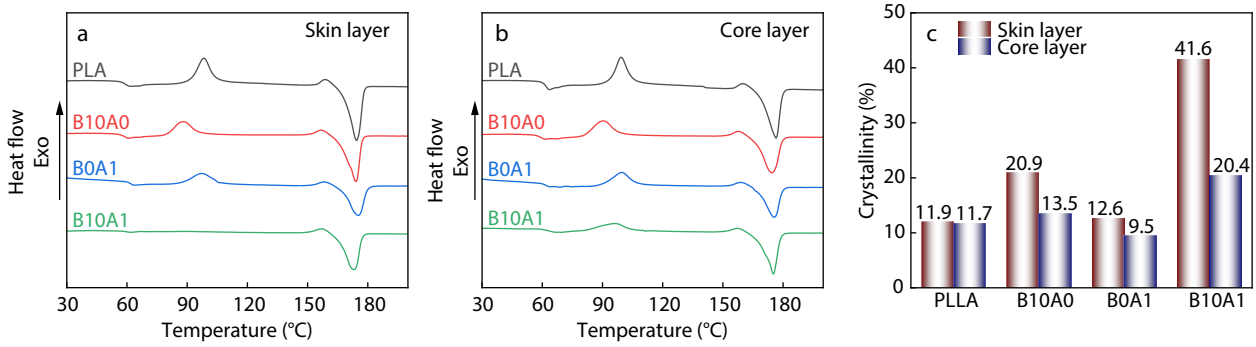

Fig. 2 DSC first heating curves of injection-molded PLA and its blend specimens for (a) the skin layer and (b) the core layer, along with (c) the corresponding crystallinity.

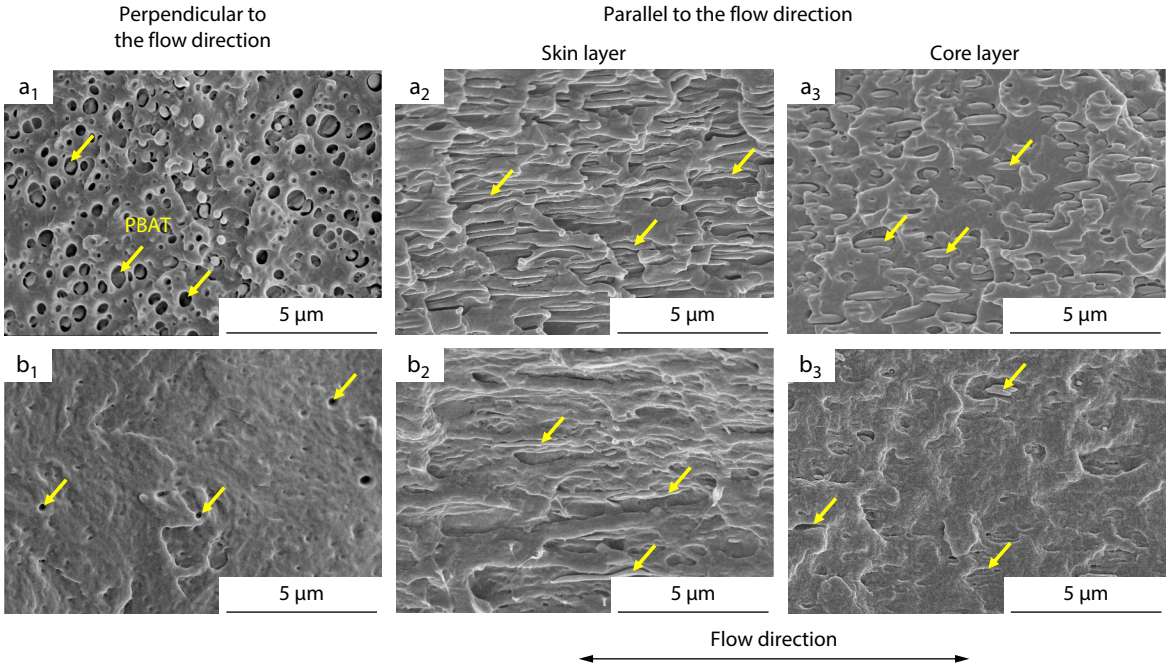

Fig. 3 SEM images of the cryo-fractured surfaces of injection-molded B10A0 (a_1–a_3) and B10A1 (b_1–b_3) specimens: (a_1, b_1) cross-sections perpendicular to the flow direction; (a_2, b_2) skin layers parallel to the flow direction; (a_3, b_3) core layers parallel to the flow direction. The PBAT phase is indicated by yellow arrows.

https://doi.org/10.1007/s10118-025-3529-x

phase interface was more diffused and the PBAT domains were smaller, resulting in a higher specific surface area. This is attributed to the presence of ADR, which induces in-situ grafting reactions between PLA and PBAT to form PLA-*co*-PBAT copolymers (as schematically illustrated in Fig. S4 in ESI), thereby markedly enhancing the interfacial compatibility. This grafting reaction was demonstrated in our previous work and is therefore not elaborated here.[18,38]

Based on morphological analysis, the anomalously high crystallinity observed in the injection-molded B10A1 specimen can be preliminarily attributed to the fibrillar structure of the PBAT phase induced by shear flow and the reduced domain size resulting from enhanced interfacial compatibility. Both factors substantially increased the specific surface area of the PBAT phase, thereby amplifying its effectiveness as a heterogeneous nucleating agent. In contrast, the adverse effect of reduced chain mobility and regularity in PLA, caused by grafting reactions—which would normally suppress the crystallization rate—appears to be less dominant in this case. On the other hand, PBAT fibrils in the skin layer exhibit a higher aspect ratio than those in the core, leading to a larger specific surface area and stronger nucleation capability. As a result, the skin layers in both the B10A0 and B10A1 specimens showed markedly higher crystallinity than the core layer. Nevertheless, the enhanced nucleating effect of PBAT should not be regarded as the only contributing factor to the high crystallinity observed in B10A1, since the skin layer of B0A1 (without PBAT) also exhibits unexpectedly higher crystallinity than neat PLA. Additional factors contributing to the enhanced crystallization of B10A1 are discussed below.

Relaxation Behavior

As the PBAT phase can form a fibrillar structure under the influence of the flow field, the PLA molecular chains are inevitably oriented along the flow direction, although this orientation gradually diminishes because of chain relaxation when the mold temperature exceeds the T_g of PLA (about 60 °C), as reported in previous studies.[29–31] Here, to confirm the presence of the initial chain orientation, a representative B10A1 specimen was analyzed using P-FTIR spectroscopy, as shown in Fig. 4(a). To prevent chain relaxation and subsequent disorientation at temperatures above T_g from affecting the analysis, the mold temperature for the sample used in P-FTIR spectroscopy was deliberately set to 30 °C. The 921 cm^{-1} band, associated with C—C backbone stretching coupled with CH_3 rocking, is regarded as specific to α crystals, while the 956 cm^{-1} band indicates the amorphous PLA phase.[35,41] Although the temperature of the B10A1 melt rapidly dropped below T_g at such a low mold temperature, the characteristic band at 921 cm^{-1} was still observed in the P-FTIR spectra, indicating the rapid crystallization capability of B10A1 under the flow field. The intensity of the 956 cm^{-1} band varied with the polarization angle and exhibited a distinct maximum, revealing that the molecular chains in the amorphous phase of PLA were oriented.[42,43] The orientation factor was calculated to be −0.096 according to Eqs. (1) and (2). The orientation of the molecular chains in the amorphous phase decreases the conformational entropy, thereby reducing the nucleation barrier and promoting chain folding and ordered pack-

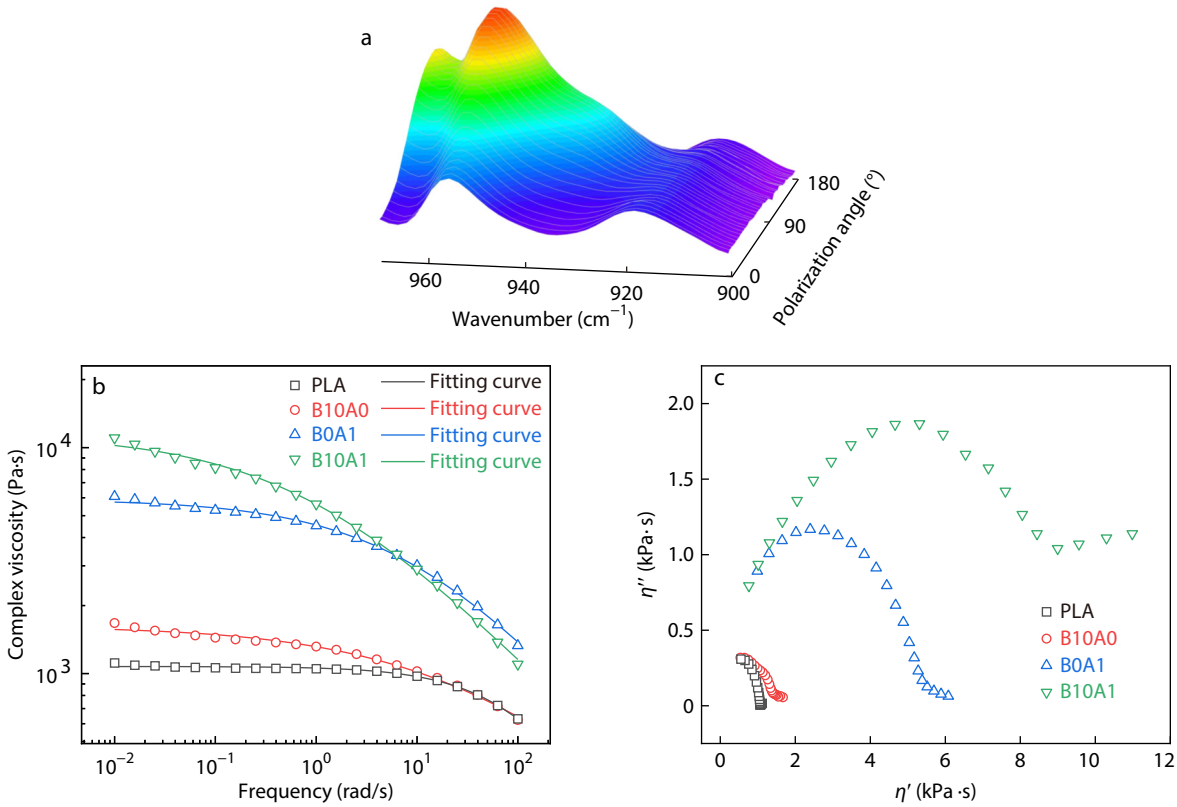

Fig. 4 (a) P-FTIR spectra of injection-molded B10A1 specimens; (b) Frequency-dependent complex viscosity with the corresponding Williamson fitting curves, and (c) Cole-Cole plots of PLA and its blends.

https://doi.org/10.1007/s10118-025-3529-x

ing, which can collectively facilitate crystallization.[29–31] However, when the mold temperature significantly exceeds PLA's T_g, such as at 100 °C, the PLA chains would undergo relaxation and gradually lose their orientation.[29,31] Accordingly, relaxation time is a critical parameter for evaluating the duration over which molecular chain orientation is maintained.

Although directly measuring the relaxation time of PLA at 100 °C is challenging because PLA is not in a molten state at this temperature, the relaxation time can be indirectly assessed by analyzing the rheological behavior of PLA and its blends at 190 °C. Fig. 4(b) presents the variation in the complex viscosity (η^*) with frequency (ω) for these samples. Higher viscosity generally corresponds to a longer relaxation time.[29,31,44] The B10A0 blend exhibited a higher complex viscosity than neat PLA, particularly at low frequencies, suggesting that the introduction of the PBAT phase suppressed PLA chain relaxation. Furthermore, both B0A1 and B10A1 show even higher complex viscosities, which is attributed to the branching of PLA molecular chains induced by ADR. The relaxation behavior of PLA and its blends was further analyzed using Cole-Cole plots of the imaginary (η'') versus real (η') components of the complex viscosity, as shown in Fig. 4(c). The radius of the arc in the Cole-Cole plot typically correlates positively with the relaxation time.[29,44] In line with the complex viscosity results, compared to neat PLA, the B10A0 blend exhibited a larger arc radius, and the ADR-containing B0A1 blend showed an even larger radius. Notably, the B10A1 blend containing both PBAT and ADR presented the largest arc radius, indicating the longest relaxation time. By fitting the data in Fig. 4(b) through the Cox-Merz transformation of complex viscosity using the Williamson empirical model $\eta = \eta_0/[1 + (\lambda\omega)^n]$,[29] the zero-shear viscosity (η_0) and relaxation time (λ) of the samples were obtained, with the relevant values listed in Table 2. The relaxation times of neat PLA, B10A0, B0A1, and B10A1 blends at 190 °C were determined as 0.006, 0.028, 0.097, and 1.087 s, respectively, which agree well with the above analyses.

Table 2 Zero shear viscosity (η_0) and relaxation time (λ) of PLA and its blends.

Sample	η_0 (Pa·s)	λ (s)
PLA	1074	0.006
B10A0	1623	0.028
B0A1	5893	0.097
B10A1	11458	1.087

The prolonged relaxation time enabled the oriented state of the PLA chains to be preserved for a longer period, thereby promoting crystallization. Accordingly, the exceptionally high crystallinity of the injection-molded B10A1 specimens can be attributed to the combined effects of the increased specific surface area of the PBAT phase, which enhanced heterogeneous nucleation and prolonged the relaxation time that sustained the oriented state of the PLA chains over an extended duration. Similarly, the higher crystallinity observed in the skin layer compared to the core layer is not solely due to the enhanced heterogeneous nucleation effect of PBAT, but is also influenced by the stronger shear flow and faster cooling rate in the skin layer, which promotes greater chain orientation. Regarding the observation that the skin-layer crystallinity of the B0A1 specimen is higher than that of neat PLA, whereas its core-layer crystallinity is lower (Fig. 2), this phenomenon can be attributed to the competition between molecular orientation and the mobility/regularity of PLA chains. Specifically, in the skin layer of B0A1, the molecular orientation plays a dominant role in promoting crystallization. In contrast, in the core layer, the relatively weak chain orientation, together with the absence of heterogeneous nucleation leads to the crystallization-inhibiting effect—stemming from reduced chain mobility and chain regularity—becoming dominant.

Crystalline Structure

To further verify the crystallization-promotion mechanism proposed above, the amorphous regions on the cryo-fractured surfaces (parallel to the flow direction) of PLA and its blends were etched to observe their crystalline morphologies by SEM. For a clearer visualization of the crystalline structures, specimens with higher crystallinity—prepared by holding in the mold for 5 min—were selected for SEM observation (Fig. 5). Neat PLA displays typical spherulites in both the skin and core regions, suggesting that owing to the short relaxation time of PLA molecular chains, extensive relaxation occurs prior to crystallization. In contrast, for B0A1, the prolonged relaxation time enabled the oriented state of the PLA chains in the skin layer to be preserved, resulting in the formation of shish-kebab structures. However, in the core layer of B0A1, where the shear field was weaker and the cooling rate was slower, the significantly weakened molecular chain orientation led to the formation of spherulites. The crystalline morphology of B10A0 resembles that of B0A1 in both the skin and core layers; the distinction lies in the shish-kebabs in the skin layer wrapped around the PBAT fibrils, indicating that oriented PLA chains stack along these fibrils, which act as nucleation sites. As expected, the improved compatibility of B10A1 gives rise to markedly finer and more numerous PBAT fibrils, which provide additional nucleation sites and consequently result in denser shish-kebabs in the skin layer. Moreover, owing to the enhanced nucleating ability of the PBAT phase and substantially extended relaxation time, the crystalline morphology in the core layer of B10A1 also exhibits a certain degree of orientation.

To further confirm the formation of oriented shish-kebab structures and quantify their degree of orientation, 2D-WAXD measurements were conducted on PLA and its blend specimens at distances of 500, 1000, and 1500 μm from the specimen surface (Fig. 6). Neat PLA exhibited an isotropic amorphous pattern at all measured distances, indicating the absence of oriented crystalline structures. In contrast, the other three samples displayed arc-shaped reflections at certain distances, suggesting the presence of oriented crystals in all of them. This phenomenon can be attributed to the extended relaxation times of the molecular chains. However, as the distance from the specimen surface increases, the diffraction arcs weaken or disappear. For instance, B0A1 showed no diffraction arcs at 1000 and 1500 μm, while B10A0 exhibited weaker diffraction arcs at 1000 μm and none at 1500 μm. This behavior was due to the weaker shear flow and slower cooling farther from the surface, which reduced the molecular chain orientation and hindered the formation of oriented

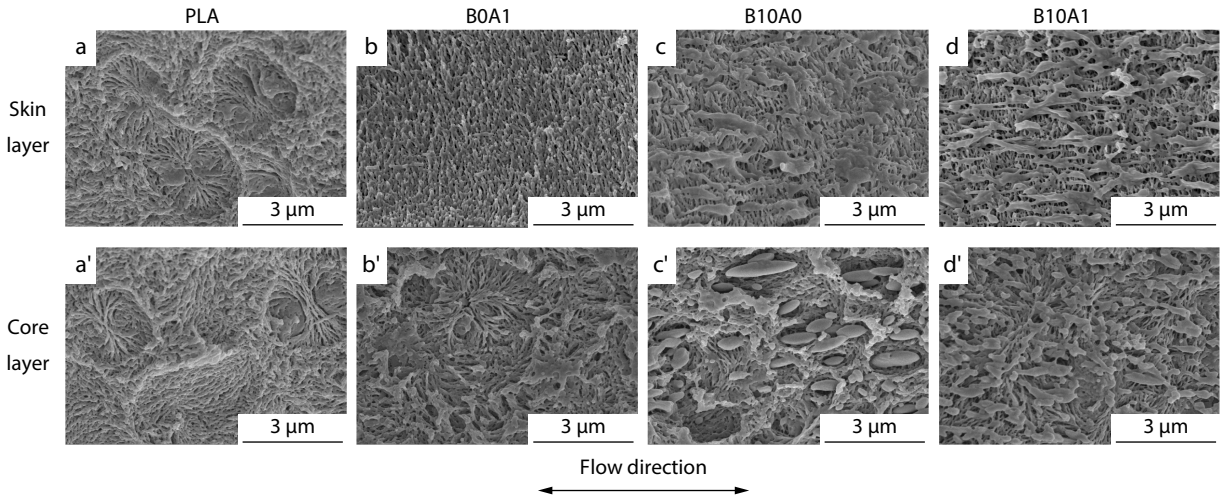

Fig. 5 SEM images showing the crystalline morphology of (a, a') PLA, (b, b') B0A1, (c, c') B10A0, and (d, d') B10A1 specimens parallel to the flow direction. Images (a–d) and (a'–d') correspond to the skin and core layers, respectively.

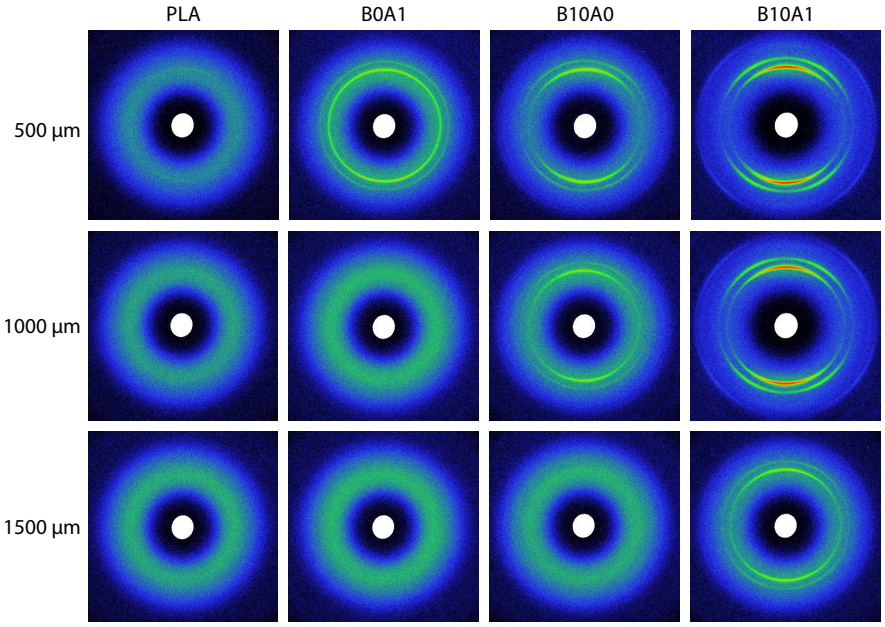

Fig. 6 2D-WAXD patterns of PLA, B0A1, B10A0, and B10A1 specimens at distances of 500, 1000, and 1500 μm from the specimen surface.

crystals. Notably, owing to the markedly prolonged relaxation time and significantly enhanced nucleating ability of the refined PBAT fibrils, B10A1 exhibited stronger diffraction signals at both 500 and 1000 μm, and arc-shaped reflections remained visible even at 1500 μm.

Herman's orientation factor and orientation degree were calculated from the azimuthal variation of the (200/110) reflection intensity (Figs. 7a–7c), and the resulting values are presented in Fig. 8. Clearly, B10A1 exhibited the highest Herman's orientation factor (0.22) and orientation degree (46.9%) at all measured distances from the specimen surface. Moreover, at 1500 μm from the specimen surface (*i.e.*, in the core layer), B10A1 still showed a Herman's orientation factor of 0.05 and an orientation degree of 11.7%, consistent with the SEM observations described above. Remarkably, although B10A0 had a shorter relaxation time than B0A1, as reflected by its rheological behavior, it exhibited a higher degree of orientation. This likely results from the nucleating effect of the PBAT fibrils, which promotes the rapid crystallization of a fraction of PLA chains before full relaxation, thereby preserving their oriented state. In addition, rapidly formed crystals can increase the melt viscosity, further prolonging the relaxation time.[45] The corresponding 1D-WAXD patterns, obtained by circular integration of the 2D-WAXD data are presented in Figs. 7(d)–7(f). Evidently, B10A1 displays the highest peak intensity, indicating the highest crystallinity. Furthermore, the decrease in peak intensity with increasing distance from the specimen surface indicates lower crystallinity near the core layer, which is consistent with the crystallinity results obtained from DSC measurements.

The effect of PBAT content on the crystallinity of the injection-molded PLA/PBAT/ADR specimens (1 phr ADR) was further investigated by DSC (Fig. S5 in ESI), with the first-heating DSC curves of B0A1 and B10A1 shown in Fig. 2. The results

clearly indicate that crystallinity increases with the PBAT content in both the skin and core layers. This enhancement can be attributed to two factors: first, a higher PBAT content provides more nucleation sites; second, the relaxation time of the blend melt increases with the PBAT content, as evidenced by the rheological behavior (Fig. 4 and Fig. S6 in ESI).

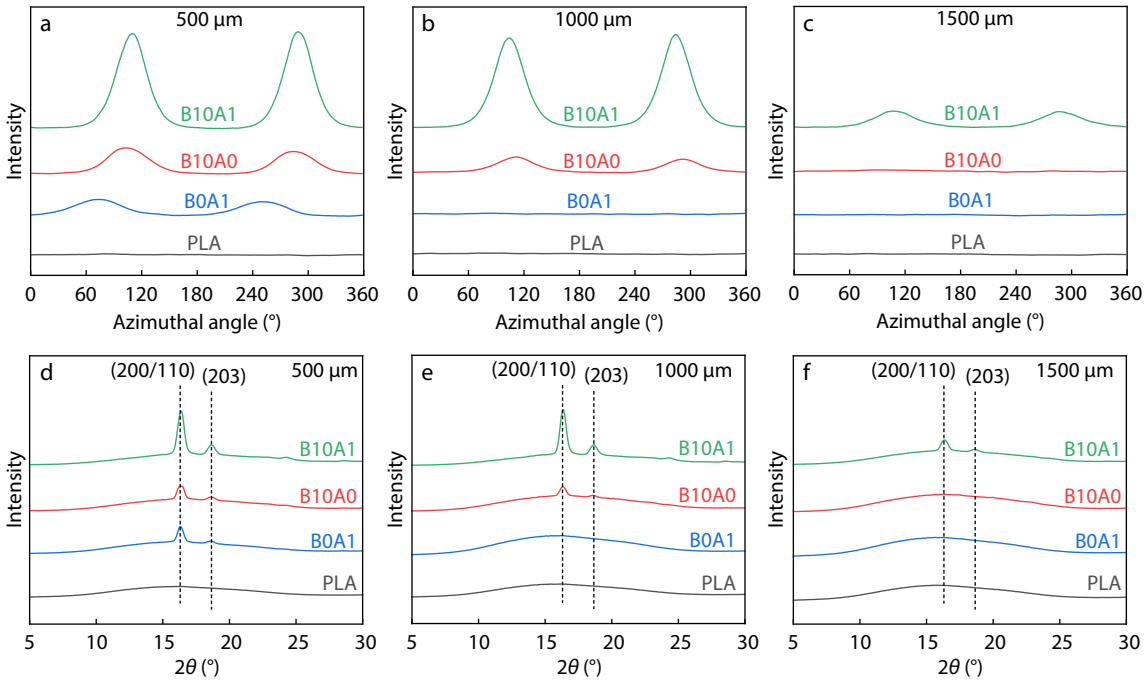

Fig. 7 (a–c) Variation in the (200/110) reflection intensity as a function of azimuthal angle (0°–360°), and (d–f) 1D-WAXD patterns for PLA and its blend specimens at distances of 500, 1000, and 1500 μm from the specimen surface, respectively.

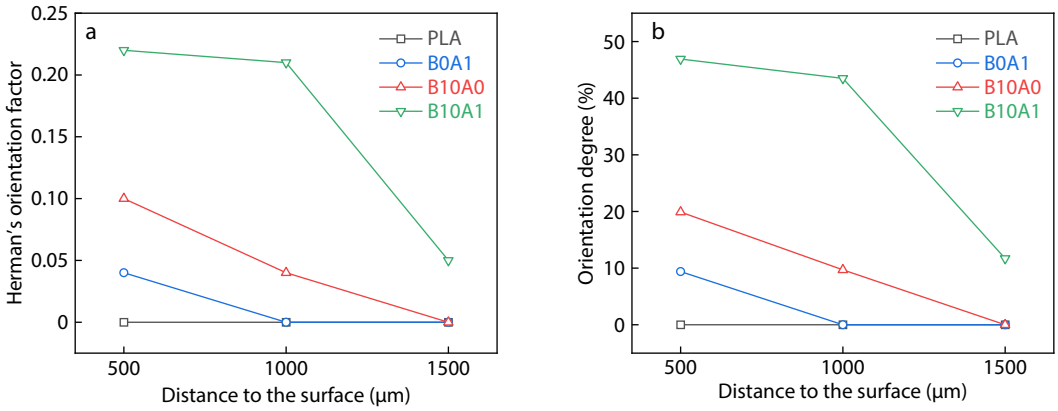

Fig. 8 (a) Herman's orientation factor and (b) orientation degree of PLA and its blend specimens as a function of distance from the specimen surface.

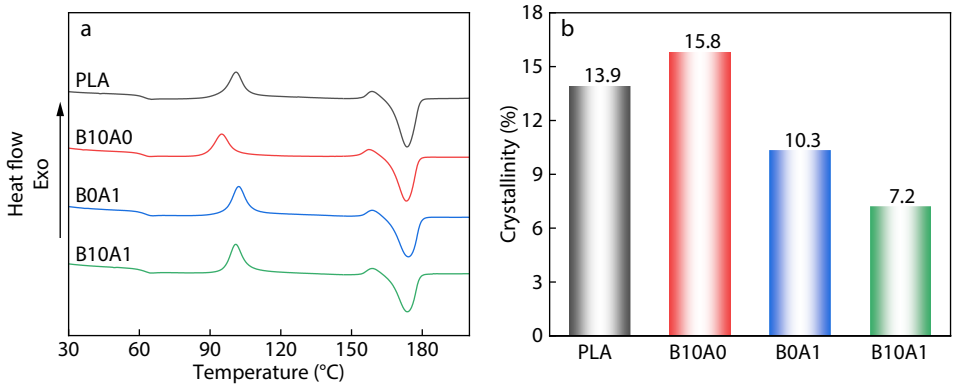

https://doi.org/10.1007/s10118-025-3529-x

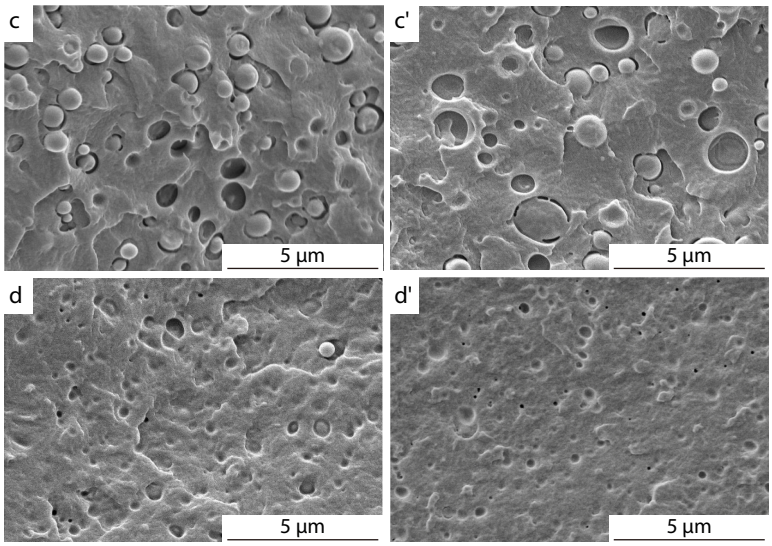

Fig. 9 (a) DSC first heating curves of the compression-molded PLA and its blends, and (b) the corresponding crystallinity. SEM images of the (c, d) cross-sections and (c′, d′) longitudinal sections of the compression-molded specimens: (c, c′) B10A0 and (d, d′) B10A1.

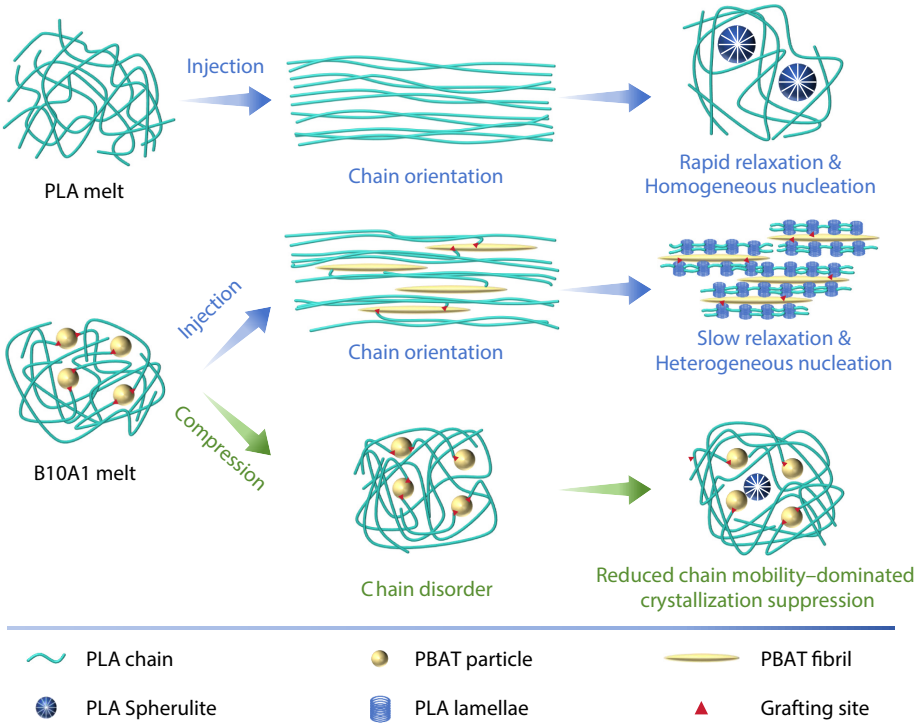

Fig. 10 Schematic illustration of the crystallization behavior of PLA and B10A1 blend during injection and compression molding.

Crystallinity of Compression-Molded Specimens

To further verify that the high crystallinity of the B10A1 sample originated from the shear flow generated during injection molding, B10A1 and its reference samples were also prepared *via* compression molding for comparison. After hot pressing at 200 °C, the samples were quenched to 100 °C, held isothermally for 2 min to allow crystallization, and then cooled to room temperature. Fig. 9(a) shows the first-heating DSC curves of the compression-molded samples, with the corresponding crystallinity presented in Fig. 9(b). The crystallinity order among the samples was consistent with the isothermal crystallization rate determined by DSC (Fig. 1). For instance, B10A1, which exhibited the slowest crystallization rate at 100 °C in the DSC measurement, accordingly shows the lowest crystallinity of 7.2% in the compression-molded sample, markedly lower than that of its injection-molded counterpart. This result indicates the absence of shear-flow-induced acceleration of crystallization in the compression molding process. SEM images (Figs. 9c–9d′) further support this observation, showing that in both the cross-sectional and longitudinal views of the B10A0 and B10A1 compression-molded samples, the PBAT phase exhibits a typical spherical morphology rather than a fibrillar morphology. It is notewor-

thy that the PBAT domains in the compression-molded samples were significantly larger than those in the cross-sections perpendicular to the flow direction of the injection-molded samples (Figs. $3a_1$ and $3b_1$). This can be attributed to the fibrillation of the PBAT phase during injection molding, which generates elongated fibrils with reduced diameters.

Based on these findings, the mechanism by which shear flow during injection molding markedly enhances the crystallization of B10A1 is illustrated in Fig. 10. Although the molecular chains of neat PLA become oriented under shear flow, their short relaxation time leads to rapid disorientation, resulting in the formation of random coils. Together with the absence of heterogeneous nucleation sites, this results in a slow crystallization rate. In contrast, in the B10A1 blend, the PBAT phase transforms from spherical to fibrillar under shear flow, while reactive compatibilization further refines the fibrils, significantly increasing their specific surface area and thereby enhancing heterogeneous nucleation. Furthermore, reactive compatibilization prolongs the relaxation time of PLA chains, allowing the oriented state to persist for a longer period. The synergistic effects of these factors markedly accelerate the crystallization of PLA. However, under static conditions, such as compression molding, where PBAT remains spherical and PLA chains lack orientation, the reduced mobility and structural regularity of PLA induced by reactive compatibilization become the dominant factors, thereby suppressing crystallization.

CONCLUSIONS

In summary, reactive compatibilization was found to promote PLA crystallization in PLA/PBAT blends under shear flow, and the underlying mechanism was elucidated. DSC isothermal crystallization results revealed that under static conditions, reactive compatibilization markedly suppressed PLA crystallization by reducing chain mobility and regularity. However, crystallinity measurements of the injection-molded specimens showed that the reactive compatibilized blends exhibited significantly higher crystallinity in both the skin and core layers. SEM observations indicated that the PBAT domains transformed from spherical to fibrillar structures under shear flow, while reactive compatibilization further refined these fibrils, greatly increasing their specific surface area and thereby enhancing heterogeneous nucleation. Rheological analysis demonstrated that reactive compatibilization extended the relaxation time of PLA chains, thereby maintaining their orientation for a longer period. These two effects jointly facilitated PLA crystallization. Furthermore, SEM and 2D-WAXD analyses confirmed the formation of shish–kebab structures with a higher degree of orientation in the reactive compatibilised blends, validating the proposed crystallization mechanism. This study elucidates the crystallization characteristics of reactive compatibilized blends under shear flow, thereby expanding the understanding of their crystallization behavior.

Conflict of Interests

The authors declare no interest conflict.

Electronic Supplementary Information

Electronic supplementary information (ESI) is available free of charge in the online version of this article at http://doi.org/10.1007/s10118-025-3529-x.

Data Availability Statement

The data supporting the findings of this study are available from the corresponding author upon reasonable request.

ACKNOWLEDGMENTS

This work was financially supported by the National Natural Science Foundation of China (No. 52573053).

REFERENCES

1 Zhou, X. W.; Huang, J.; Zhang, X. H.; Li, T.; Wang, Y.; Wang, S. B.; Xia, B. H.; Dong, W. F. Design of tough, yet strong, heat-resistant PLA/PBAT blends with reconfigurable shape memory behavior by engineering exchangeable covalent crosslinks. *Chinese J. Polym. Sci.* **2023**, *41*, 1868–1878.
2 Sun, D. X.; Huang, C. H.; Zhang, Z. X.; Lan, Z. Y.; Zha, Y. F.; Wang, A. Y.; Guo, L.; Wang, Y. Synchronously enhancing fracture toughness and mechanical strength of polyester blend composites via constructing dual-network structures of one-dimensional carbon nanofillers. *Polymer* **2025**, *324*, 12.
3 Shou, T.; Dong, Q. S.; Yin, D. X.; Hu, S. K.; Zhao, X. Y.; Zhang, L. Q. Super-tough polylactic acid blends via tunable dynamic vulcanization of biobased polyurethanes. *Compos. Pt. B-Eng.* **2024**, *276*, 10.
4 Yang, R.; Cai, C. Y.; Han, X. C.; Chen, Z. F.; Gu, G. Z.; Zhang, C. P.; Zou, G. X.; Li, J. C. Supertough and biodegradable poly(lactic acid) blends with "hard-soft" core-shell unsaturated poly(ether-ester) through self-vulcanization. *Macromolecules* **2023**, *56*, 7271–7285.
5 Xiao, J.; Wu, M. H.; Ma, W. Y.; Bing, X. H.; Wang, L.; Zheng, W. E.; Xiong, D. L. Achieving high impact toughness in injection-molded SMMA foams via the synergistic effects of cell size and SBS. *Polymer* **2024**, *313*, 10.
6 Wang, D. F.; Liu, B.; Niu, D. Y.; Yang, W. J.; Zhang, X.; Xu, P. W.; Ma, P. M. Strong, ductile and transparent biaxially oriented poly(lactic acid) with low content of poly(3-hydroxybutyrate-co-3-hydroxyhexanoate) by temperature-gradient stretching: the role of mesophase. *Compos. Commun.* **2025**, *55*, 102311.
7 Wu, B. G.; Yang, W. J.; Niu, D. Y.; Dong, W. F.; Chen, M. Q.; Liu, T. X.; Du, M. L.; Ma, P. M. Stereocomplexed poly(lactide) composites toward engineering plastics with superior toughness, heat resistance and anti-hydrolysis. *Chinese J. Polym. Sci.* **2020**, *38*, 1107–1116.
8 Cao, Y.; Xu, P. W.; Yang, W. J.; Zhu, X. M.; Dong, W. F.; Chen, M. Q.; Du, M. L.; Liu, T. X.; Lemstra, P. J.; Ma, P. M. UV resistant PBT nanocomposites by reactive compatibilization and selective distribution of tailor-made double-shelled TiO_2 nanohybrids. *Compos. Pt. B-Eng.* **2021**, *205*, 11.
9 Li, C. Y.; Shi, B.; Jiang, J.; Lin, H. X.; Xu, Y. C.; Lin, S. L.; Zhao, L.; Meng, X.; Xi, Z. H. Revisiting the effect of constructing stereocomplex crystallites through a compatibilizer in super tough PLLA blends. *Macromolecules* **2025**, *58*, 4407–4418.
10 Yokoyama, K.; Guan, Z. B. A vitrimer acts as a compatibilizer for polyethylene and polypropylene blends. *Angew. Chem.-Int. Edit.*

Graphical Abstract

Revisiting the Effect of Reactive Compatibilization on Polymer Crystallization: From Static Suppression to Shear-Induced Promotion

Bao-Gou Wu, Xiao-Hu Bing, Qian Ren, Lan Ding, Ji-Zhang Li, Wen-Ge Zheng, and Long Wang

Ningbo Institute of Materials Technology and Engineering, Chinese Academy of Sciences; University of Chinese Academy of Sciences

Reactive compatibilization typically suppresses crystallization in polymer blends by reducing chain mobility and regularity, but this study reveals that under shear flow it instead significantly enhances the crystallization rate.

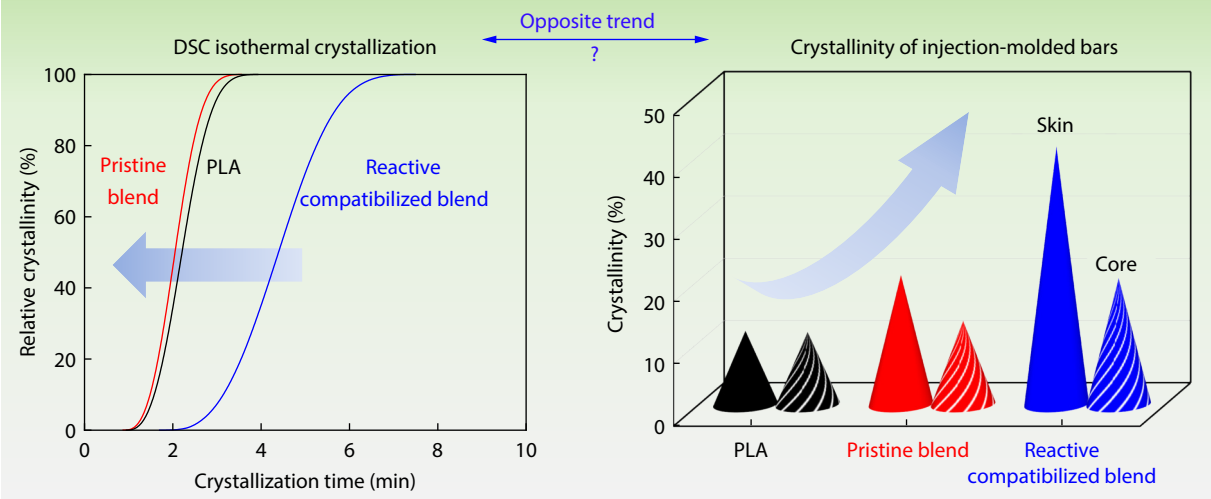

Chinese J. Polym. Sci. 2026, 44, 756–767 *https://doi.org/10.1007/s10118-025-3529-x*

2024, *63*, 5.

11 Guan, J. Y.; Liu, J. L.; Zhu, X. M.; Yang, W. J.; Niu, D. Y.; Xu, P. W.; Ma, P. M. Molecularly engineered Janus nanosheets dual-anchored interfaces for multifunctional polylactic acid blends in intelligent packaging. *Chem. Eng. J.* **2025**, *523*, 168383.

12 Wu, M. H.; Ren, Q.; Li, X. Y.; Gao, P.; Wang, L.; Zheng, W. G.; Cui, P.; Yi, X. S.; Yang, W. Supertough polylactide blend foams with controlled cell size. *Macromolecules* **2024**, *57*, 10432–10441.

13 Wu, B. G.; Xu, P. W.; Yang, W. J.; Hoch, M.; Dong, W. F.; Chen, M. Q.; Bai, H. Y.; Ma, P. M. Super-toughened heat-resistant poly(lactic acid) alloys by tailoring the phase morphology and the crystallization behaviors. *J. Polym. Sci.* **2020**, *58*, 500–509.

14 Qu, Y. D.; Rong, C. Y.; Ling, X. Y.; Wu, J. L.; Chen, Y. H.; Wang, H. T.; Li, Y. J. Role of interfacial postreaction during thermal treatment: toward a better understanding of the toughness of PLLA/reactive elastomer blends. *Macromolecules* **2022**, *55*, 1321–1331.

15 Xie, L. Z.; Xie, Y. Y.; Wu, Q. H.; Wang, M. Z.; Wu, Q. C.; Zhou, X.; Ge, X. W. Effect of poly(acrylic acid)-modified poly(ethylene terephthalate) on improving the integrated mechanical properties of poly(ethylene terephthalate)/elastomer blend. *Ind. Eng. Chem. Res.* **2015**, *54*, 4748–4755.

16 Chen, Y. K.; Wang, W. T.; Yuan, D. S.; Xu, C. H.; Cao, L. M.; Liang, X. Q. Bio-based PLA/NR-PMMA/NR ternary thermoplastic vulcanizates with balanced stiffness and toughness: "soft-hard" core-shell continuous rubber phase, in situ compatibilization, and properties. *ACS Sustain. Chem. Eng.* **2018**, *6*, 6488.

17 Wu, B. G.; Zeng, Q. T.; Niu, D. Y.; Yang, W. J.; Dong, W. F.; Chen, M. Q.; Ma, P. M. Design of supertoughened and heat-resistant PLLA/elastomer blends by controlling the distribution of stereocomplex crystallites and the morphology. *Macromolecules* **2019**, *52*, 1092–1103.

18 Wu, B.; Gao, M.; Bing, X.; Xiao, J.; Cao, Y.; Zheng, W.; Wang, L. Multiple synergies for enhancing the toughening efficiency: toward fully biodegradable polylactide-based engineering plastics with superior toughness, strength and heat resistance. *Polymer* **2025**, *335*, 128846.

19 Chen, J. L.; Rong, C. Y.; Lin, T. T.; Chen, Y. H.; Wu, J. L.; You, J. C.; Wang, H. T.; Li, Y. J. Stable co-continuous PLA/PBAT blends compatibilized by interfacial stereocomplex crystallites: toward full biodegradable polymer blends with simultaneously enhanced mechanical properties and crystallization rates. *Macromolecules* **2021**, *54*, 2852–2861.

20 Wei, D. Y.; Chen, N.; Yin, Z. W.; Li, Y. B.; Zheng, G. F.; Bian, J. J.; Pan, H. W.; Wang, G. Q.; He, L. T.; Zhao, Y. Crystallization properties, heat resistance, and hydrolytic resistance of poly(L-lactide)/poly(D-lactide) blend enhanced by in situ formation of stereocomplex polylactide. *Chinese J. Polym. Sci.* **2025**, *43*, 1549–1564.

21 Wang, W. Y.; Wang, X. H.; Wang, Z. G. Ultrahigh strength and toughness of polylactide added with EGMA elastomer of a small amount processed via pressure-induced flow above the glass transition temperature. *Appl. Surf. Sci.* **2024**, *665*, 12.

22 Li, X.; Lv, B. H.; Wang, H. T.; Zhang, X. H.; Huang, J.; Li, T.; Wang, S. B.; Dong, W. F. Stiffening and toughening rigid polymers through

controllable stress concertation induced by hard-hard dual nanophases. *ACS Macro Lett.* **2025**, *14*, 1107–1113.
23 Liu, B.; Xu, P. W.; Niu, D. Y.; du Sart, G. G.; Shi, Y. Q.; Joziasse, K.; Zhou, Y. X.; Ma, Y.; Yang, W. J.; Zhang, X.; et al. Superior ductile and barrier PLA/PGA films by an in situ constructing transversely isotropic network and well-ordered crystalline nanolayers. *Macromolecules* **2025**, *58*, 1717–1727.
24 Ye, H. S.; Li, C. J.; Zhang, Y.; Xia, Y.; Wang, H. T.; Li, Y. J. Formation of an organic rigid core-soft shell structure based on the melting temperature difference between the core and the matrix by reactive processing: a facile strategy for highly efficient polymer toughening. *Macromolecules* **2025**, *58*, 1223–1234.
25 Bao, W.; Gao, Y. B.; Zhang, J. N.; Jin, J.; Zhang, N.; Liu, B. J.; Zhang, M. Y.; Su, Z. H.; Liang, H. W.; Ji, X. L.; et al. Biodegradable poly (lactic acid) blends toughened with in situ formed core-shell structure by reactive processing. *Polymer* **2025**, *326*, 10.
26 Gong, Z.; Huang, J. R.; Fan, J. F.; Chen, X. Q.; Wang, H.; Chen, Y. K. A super-toughened poly(lactic acid)-based thermoplastic vulcanizate through incorporating modified SiO_2 nanoparticles. *Compos. Sci. Technol.* **2022**, *226*, 13.
27 Chen, Y. K.; Yuan, D. S.; Xu, C. H. Dynamically vulcanized biobased polylactide/natural rubber blend material with continuous cross-linked rubber phase. *ACS Appl. Mater. Interfaces* **2014**, *6*, 3811–3816.
28 Guan, J. Y.; Ding, N.; Xu, P. W.; Yang, W. J.; Niu, D. Y.; Zhang, X.; Liu, T. X.; Ma, P. M. Synchronous toughening, strengthening, and ultraviolet resistance of immiscible polylactic acid/polypropylene carbonate blends compatibilized by a low threshold of reactive janus nanosheets. *Macromolecules* **2024**, *57*, 11407–11416.
29 Ma, Y.; Niu, D. Y.; Liu, J. L.; Liu, B.; Xu, P. W.; Jiao, X. C.; Yang, W. J.; Liu, T. X.; Ma, P. M. Branching-density dependent chain relaxation and orientated crystallization behavior of the stretched polylactic acid melt. *Macromolecules* **2025**, *58*, 5674–5687.
30 Sang, Z. H.; Xie, X. L.; Zhou, S. Y.; Li, Y.; Yan, Z.; Xu, L.; Zhong, G. J.; Li, Z. M. Gradient structure of crystalline morphology in injection-molded polylactide parts tuned by oscillation shear flow and its influence on thermomechanical performance. *Ind. Eng. Chem. Res.* **2017**, *56*, 6295–6306.
31 Zhou, S. Y.; Niu, B.; Xie, X. L.; Ji, X.; Zhong, G. J.; Hsiao, B. S.; Li, Z. M. Interfacial shish-kebabs lengthened by coupling effect of in situ flexible nanofibrils and intense shear flow: achieving hierarchy to conquer the conflicts between strength and toughness of polylactide. *ACS Appl. Mater. Interfaces* **2017**, *9*, 10148–10159.
32 Wang, W. Y.; Luo, J. H.; Wang, X. H.; Wang, Z. G. Tensile deformation above the glass transition temperature to construct a crystalline microfibrillar superstructure for achieving supertough, ultrastrong, and transparent neat polylactide. *Macromolecules* **2025**, *58*, 4419–4437.
33 Xie, Y. P.; Xiong, H. A.; Zheng, Z.; Zhang, L. F.; Chen, Y. H. Facile and scalable fabrication of high-performance polylactide-based medical microparts through combining the microinjection molding intense shear stress field and annealing strategy. *Ind. Eng. Chem. Res.* **2022**, *61*, 13886–13897.
34 Tabatabaei, S. H.; Carreau, P. J.; Ajji, A. Microporous membranes obtained from polypropylene blend films by stretching. *J. Membr. Sci.* **2008**, *325*, 772–782.
35 Zhang, J. M.; Tsuji, H.; Noda, I.; Ozaki, Y. Weak intermolecular interactions during the melt crystallization of Poly(L-lactide) investigated by two-dimensional infrared correlation spectroscopy. *J. Phys. Chem. B* **2004**, *108*, 11514–11520.
36 Wei, X. F.; Bao, R. Y.; Cao, Z. Q.; Yang, W.; Xie, B. H.; Yang, M. B. Stereocomplex crystallite network in asymmetric PLLA/PDLA blends: formation, structure, and confining effect on the crystallization rate of homocrystallites. *Macromolecules* **2014**, *47*, 1439–1448.
37 Jiang, L.; Wolcott, M. P.; Zhang, J. W. Study of biodegradable polyactide/poly(butylene adipate-co-terephthalate) blends. *Biomacromolecules* **2006**, *7*, 199–207.
38 Wu, M. H.; Ren, Q.; Zhu, X. Y.; Li, W. W.; Luo, H. B.; Wu, F.; Wang, L.; Zheng, W. E.; Cui, P.; Yi, X. S. Super toughened blends of poly(lactic acid) and poly(butylene adipate-co-terephthalate) injection-molded foams via enhancing interfacial compatibility and cellular structure. *Int. J. Biol. Macromol.* **2023**, *245*, 11.
39 Bing, X. H.; Wu, M. H.; Ma, W. Y.; Xu, M. X.; Zhou, X.; Wang, L.; Zheng, W. G. Development of toughened and heat-resistant biodegradable injection-molded polylactide acid-based blend foams via enhancing interfacial bonding and PLA phase crystallization. *Polymer* **2024**, *298*, 12.
40 Ding, W. W.; Chen, Y. H.; Liu, Z.; Yang, S. In situ nano-fibrillation of microinjection molded poly(lactic acid)/poly(ε-caprolactone) blends and comparison with conventional injection molding. *RSC Adv.* **2015**, *5*, 92905–92917.
41 Zhang, J.; Tsuji, H.; Noda, I.; Ozaki, Y. Structural changes and crystallization dynamics of poly(L-lactide) during the cold-crystallization process investigated by infrared and two-dimensional infrared correlation spectroscopy. *Macromolecules* **2004**, *37*, 6433–6439.
42 Zhou, S. Y.; Huang, H. D.; Ji, X.; Yan, D. X.; Zhong, G. J.; Hsiao, B. S.; Li, Z. M. Super-robust polylactide barrier films by building densely oriented lamellae incorporated with ductile in situ nanofibrils of poly(butylene adipate-co-terephthalate). *ACS Appl. Mater. Interfaces* **2016**, *8*, 8096–8109.
43 Lin, H.; Chen, Y.; Gao, X. R.; Xu, L.; Lei, J.; Zhong, G. J.; Li, Z. M. Transparent, heat-resistant, ductile, and self-reinforced polylactide through simultaneous formation of nanocrystals and an oriented amorphous phase. *Macromolecules* **2023**, *56*, 2454–2464.
44 Fang, F. N.; Niu, D. Y.; Xu, P. W.; Liu, T. X.; Yang, W. J.; Wang, Z. Y.; Li, X. A.; Ma, P. M. A quantitative study on branching density dependent behavior of polylactide melt strength. *Macromol. Rapid Commun.* **2023**, *44*, 2200858.
45 Bing, X. H.; Ma, W. Y.; Wu, M. H.; Gao, P.; Zhou, X.; Luo, H. B.; Wang, L.; Zheng, W. G. Lightweight, strong and high heat-resistant poly(lactide acid) foams via microcellular injection molding with self-assembly nucleating agent. *Chinese J. Polym. Sci.* **2024**, *42*, 739–750.

https://doi.org/10.1007/s10118-025-3529-x